

# In-situ surface porosity prediction in DED (directed energy deposition) printed SS316L parts using multimodal sensor fusion

Adithyaa Karthikeyan, Himanshu Balhara, Andreas K. Lianos, Abhishek Hanchate, Satish T.S. Bukkapatnam

*Wm Michael Barnes '64 Department of Industrial and Systems Engineering,  
Texas A&M University, College Station, TX 77843, USA*

## ABSTRACT

This study aims to relate the time-frequency patterns of acoustic emission (AE) and other multi-modal sensor data collected in a hybrid directed energy deposition (DED) process to the pore formations at high spatial (0.5 mm) and time (< 1ms) resolutions. Adapting an explainable AI method in LIME (Local Interpretable Model-Agnostic Explanations), certain high-frequency waveform signatures of AE are to be attributed to two major pathways for pore formation in a DED process, namely, spatter events and insufficient fusion between adjacent printing tracks from low heat input. This approach opens an exciting possibility to predict, in real-time, the presence of a pore in localized surface segments (voxels) as they are printed, a major leap forward compared to prior efforts. Experiments for this study were performed on an OPTOMECH LENS®500 smart hybrid machine at Texas A&M University. Synchronized multimodal data, including force, AE, vibration and temperature were gathered from 14 different channels while an SS316L material sample was printed and subsequently machined. A deep convolution neural network classifier was used to identify the presence of pores on a voxel surface based on time-frequency patterns (spectrograms) of the sensor data collected during the process chain. The underlying explanations were drawn during subsequent XAI (LIME) analysis. The results suggest signals collected during DED were more sensitive compared to those from machining for detecting porosity in voxels (classification test accuracy of 87%). XAI analysis suggests that the energy captured in high frequency AE waveforms are ~33% lower for porous voxels compared to non-porous voxels, indicating a relatively lower laser-material interaction in the melt pool, and hence insufficient fusion and poor overlap between adjacent printing tracks. The porous voxels for which spatter events were prevalent during printing had about 27% higher energy contents in the high frequency AE band compared to other porous voxels. These signatures from AE signal can further the understanding of pore formation from spatter and insufficient fusion.

## KEYWORDS

Surface porosity detection, Multimodal sensor fusion, Acoustic Emission, Spatter formation, Explainable AI, Additive manufacturing

## 1. INTRODUCTION

Additive Manufacturing (AM), initially developed as a rapid prototyping technology, has proliferated into commercial use owing to its many advantages with respect to shape complexity and custom geometry compared to conventional manufacturing methods [1, 2]. Directed Energy Deposition (DED), a type of additive manufacturing process, employs a concentrated energy source usually laser powered that intersects the metal powder stream at a common focal point in the presence of an inert shield gas. DED has been used mainly to print functionally graded materials, metal-matrix composites and coatings [3]. However, some of the major challenges inherent to AM processes include relatively poor part accuracy as a result of the layering effect, dimensional control, residual stresses and occurrence of defects such as porosity/voids, keyhole and lack of fusion [4-6]. Pores can form in metal additive

manufactured components at the surface, sub-surface or between deposited layers due to a range of factors including spatter events, vacuum pore formation, an incomplete fusion of powder particles, the presence of gas within the metal powder, melt pool shrinkage during the cooling stage, a lack of proper bonding between overlapping layers, residual stress on the metal, and insufficient support structures during the build process [7]. The shape and size distribution of powder particles, ease of powder flow through the nozzle and choice of process parameters during printing play a vital role in the melting and solidification process [2]. High laser power with slow scan speed can cause the vaporized metal to exert a recoil pressure that pushes down the melt pool surface, forming narrow and deep keyholes [8, 9]. Low laser power often times lead to incomplete melting of the feedstock (metal powder) resulting in pores and defects due to lack of fusion [10]. High scan speeds can result in irregular pores and tracks due to balling effect, wherein the liquid scan track may breakdown and produce smaller spherical particles [11]. The occurrence of non-uniform temperature distribution along the interface between melt pool layers and gradient in surface tensions of spherical particles result in Marangoni flow, thereby creating a depression of liquid surface beneath the laser beam [12]. The event of any such defects can result in reduced corrosion resistance, poor surface finish and weakened mechanical strength of the AM parts.

Pores and void formations in DED processes can occur over multiple sizes ranging from few tens of micrometers to a few hundred micrometers in diameter. In this study, the composition of SS316L metal powder is assumed to be homogeneous with the particle diameter having a normal distribution with mean  $60 \mu\text{m}$  and standard deviation of  $\sim 8 \mu\text{m}$ . The process parameters (scanning speed, powder feed rate, laser power) employed in our experiments (described in Section 2.1) and the use of shielding gas results in less likelihood of pore formation due to factors such as vacuum pore formation, shrinkage and residual stress. We focus on capturing porosity at the surface of AM parts predominantly caused due to inefficient overlap between adjacent printing tracks based on hatch spacing, and the occurrence of spatter events where small droplets of molten material are expelled from the surface of the workpiece during deposition process [13]. Pore formation associated with spatter events in DED are predominantly characterized with the occurrence of small round pores/voids in the center region of printing tracks. Pang *et al.* [14] characterized the size and distribution of pores using image-based quantifiers such as circularity and roundness, and accordingly inferred the source of porosity formation. An object's circularity considers its form and smoothness, while roundness takes into account the object's ovality and aspect ratio. The closer these two characteristic values are to 1.0, the greater the resemblance to a sphere. Pores exhibiting high circularity and low degree of roundness were likely attributed to lack of fusion between successive printing tracks due to insufficient overlap. On the other hand, pores or voids exhibiting high degrees of both circularity and roundness had a strong likelihood to originate from defects like moisture evaporation or local voids after powder-layer deposition.

Currently, both ex-situ and in-situ based techniques are in practice for detecting porosity in AM parts [15]. Ex-situ methods consist of post manufacturing characterizations such as x-ray computed tomography and ultrasound scans. X-ray CT scans are expensive and time consuming in nature requiring long hours to scan even a small volume of the part. The attenuation effect and scattering nature of the ultrasound signals make it difficult to localize the occurrence of defects in parts [16]. In-situ monitoring comprises of visual inspection techniques using infrared, x-ray or thermal imaging and other vibration-based sensors such as accelerometer and acoustic emission (AE). Accuracy of infrared imaging systems

are subject to emissivity and reflectivity issues of the material under consideration and often times result in poor detection of medium and small sized pores. High speed X-ray imaging and X-ray diffraction studies for in-situ characterization of Laser Bed Powder Fusion (LBPF) process have revealed significant information about melt pool dynamics, solidification rates, phase transformation and pore formation mechanism due to keyhole at high spatial and temporal resolutions [17, 18]. Wolff *et al.* [19, 20] illustrated the use of high-speed synchrotron hard X-ray imaging to study the pore formation dynamics in DED with micrometer spatial resolution and microsecond temporal resolution. The inherent difference in the operations of DED and LPBF additive manufacturing systems alter the pore formation dynamics in each of the processes. Particle deposition was found to be the key driver behind pore formation due to lack of fusion in DED and the presence of voids between the packed particles on the powder bed was the primary reason for porosity due to lack of fusion in LPBF. Young *et al.* [21] discussed various spatter formation mechanisms in LPBF with the help of high-speed X-ray imaging and studied the effects of process conditions on the spatter formation phenomena. However, x-ray imaging in metal additive manufacturing must be carefully considered owing to several limitations, including high cost and complexity of the setup, less effective penetration ability on thicker materials, exposure to ionizing radiation, slower processing speed, limited resolution and potential interference from surrounding materials.

With advancements in computer vision and deep learning methods, several studies have been conducted to better understand the melt pool dynamics in AM processes from thermal images and detect the occurrence of any irregularities or defects in real time [22-24]. Khanzadeh *et al.* [15] employed spherical transformation and bi-harmonic interpolation techniques to convert the melt pool thermal distributions with different sizes/shapes to temperature measurements with identical support in the spherical domain. Based on the similarity of the thermal signatures, they were able to group similar melt pools into the same category using a self-organizing map (SOM) algorithm. Tang *et al.* [25] presented a geometry-based simulation to predict porosity caused by insufficient overlap of melt pools (lack of fusion) for changes in LPBF process parameters. However, thermal imaging systems generate tremendous amounts of data, so as to printing a small single track thin wall may result in over 10 GB of thermal image data. The signal-to-noise ratio of these thermal images may be low at times resulting in poor demarcation of the melt pool boundary. Size and center of melt pools vary during the build requiring additional precaution to align the melt pools and account for various melt pool sizes. On the other hand, high sensitivity of AE sensors and relatively inexpensive hardware offer attractive alternate solutions for real time in-situ quality monitoring of AM processes. They provide high temporal resolutions and fast processing times owing to the 1D nature of the signal compared to 2D imaging and 3D tomography data [26].

Gaja and Liou investigated the ability of AE sensor to detect and identify defects, specifically cracks and pores, generated during Laser Metal Deposition using a logistic regression (LR) model and an artificial neural network (ANN) employing statistical features of the signal such as peak amplitude, rise time, duration, energy, and number of counts. They correlated the occurrence of AE signals with shorter decay time and less amplitude to surface porosities, while cracks triggered the AE signals with shorter durations and higher amplitudes. They found signal energy to be the most important feature significantly contributing to the defect classification [27]. Taheri *et al.* [28] presented a K-means clustering methodology using spectral features of acoustic waveforms to study signatures for classifying different process conditions involved in DED additive manufacturing of Ti-6AL-4V samples. They compared the efficiency in classifying low power, low powder and powder spray process conditions against normal baseline conditions using low

frequency and high frequency bands and achieved an accuracy of about 87%. Shevchik *et al.* [26] employed spectral convolutional neural networks on the features extracted from acoustic signals consisting of relative energies of the narrow frequency bands of the wavelet packet transform. Their classifier was trained to differentiate the acoustic features of dissimilar sections of the printed part characterized by the concentration of pores, and achieved an accuracy varying between 83 and 89%. Ita *et al.* [29] developed a method for real-time monitoring of microdefects generation in Hastelloy X during selective laser melting (SLM) by using proprietary battery-powered equipment capable of continuous recording and wireless transmission of AE waveforms. They observed signatures in AE signal pertaining to pores, cracks, defects occurring after laser irradiation and due to turning back of the irradiation. Gauder *et al.* [30] presented an in-process pore detection method during machining operations on additively manufactured test pieces with cavities. They used a structure-borne acoustic sensor and analyzed its signals in both time and frequency domain using deep learning.

An overview of various machine learning based approaches in literature employed towards the prediction of surface porosity in AM parts is presented in Table 1A (refer Appendix). Though many models have come up to predict porosity in AM parts, they predominantly use experimental data to learn purely 'black box' models. As a result, they cannot be generalized beyond the training sets and lack the explanatory power to help understand the underlying physical phenomena. New class of explainable-AI (XAI) approaches help uncover these underlying physical processes and complement the predictions from powerful machine learning models [16, 31, 32]. The emergence of Industry 4.0 over the last decade has seen manufacturing industries transforming themselves by integrating physical production and operations with smart digital technologies and big data, thereby creating a highly interconnected network of manufacturing devices resulting in efficient and automated production workflows [33, 34]. The increasing use of sensor-fusion based technologies in manufacturing, wherein data from multiple sensors are fused to produce reliable information, yields a more robust understanding of the physics behind manufacturing processes and significantly contribute towards improving product quality control [35-38]. Smart manufacturing multiplex conceptualized by Bhaskar *et al.* [39] demonstrated the capability to execute multiple process chains in-situ using hybrid machine tools consisting of additive and subtractive processes integrated with high resolution sensors enabling tracking of spatiotemporal evolution of the process states.

The contributions of this study can be summarized as follows: We adapt an explainable AI (XAI) based approach using LIME (Local Interpretable Model-Agnostic Explanations) to predict and explain the occurrence of surface porosity in hybrid DED-printed SS316L components in-situ, that predominantly develops from insufficient fusion between adjacent printing tracks due to low heat input and the occurrence of spatter events during DED. Time-frequency patterns (spectrograms) of AE and accelerometer signals collected during the hybrid process chain comprising of multiple printing and milling cycles were used to predict the occurrence of porosity in localized surface segments of dimension 0.5 mm (voxels). LIME paves a way to identify dominant frequency bands from signal spectrograms that contribute towards the correct classification of porous voxels. We find signals collected during printing cycles to be more sensitive compared to those from machining to detect porosity in voxels, achieving a classification test accuracy of over 87%. Indeed, the pore structure of the printed and finished component is likely to be much different due to interlayer material transfer and adjustment during the process chain. The robust multimodal sensor data alignment allowed inferences from LIME model to be verified and crosschecked using thermal images of the melt pool, providing a means to

better understand the nature of spatter events during printing cycles that result in the occurrence of surface porosity in voxels. The rest of this paper is organized as follows: Section 2 describes the smart hybrid manufacturing (SHM) implementation at Texas A&M University and the formulation of surface porosity prediction as a binary classification problem; Section 3 explains the mathematical representation of our XAI approach using LIME; Section 4 describes CNN model performance and XAI fused thermal image inferences on the nature of spatter events that result in surface porosity followed by conclusions in Section 5.

## 2. EXPERIMENTATION

### 2.1. Smart Hybrid Manufacturing Implementation

Texas A&M smart manufacturing implementation consists of an Optomec LENS MTS 500 hybrid machine, capable of both additive and in-situ finishing operations. It uses laser powered directed energy deposition (DED) 3D printing technology and also contains a vertical rotating spindle to perform machining, grinding and polishing processes. The machine offers a build volume of 350 x 325 x 500 mm and can produce low-cost parts at approximately one-third the price of those that employ powder bed fusion 3D printing technology in terms of equipment cost, powder cost, as well as throughput. The hybrid machine has been equipped with various commercial-off-the-shelf (COTS) and image-based sensors, capable of simultaneously collecting 13+ different data streams, thereby enabling real time monitoring across various processes. Prominent ones include accelerometer, acoustic emission, thin-film force sensor, optical camera, high-speed camera and melt pool / thermal sensor. Figure 1 illustrates the multimodal sensors array that is equipped with the DED hybrid machine.

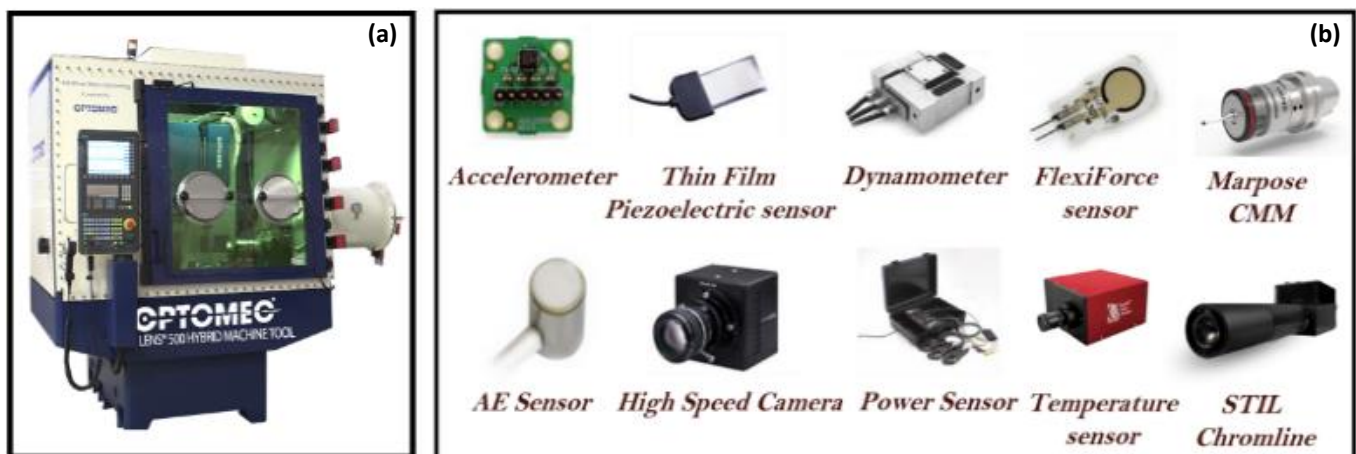


**Figure 1:** (a) Optomec DED Hybrid Machine (b) Multimodal sensors array equipped with the DED Hybrid Machine

The experiments consisted of printing cuboidal SS316L parts with dimensions 10 x 10 x 5 mm on the Optomec LENS MTS 500 Hybrid Machine Tool with different laser power and scan speed combinations as indicated in Figure 2. The sample under consideration for this study was built using a laser power of 250 watts, powder flow rate of 4 rpm and printing scan speed of 10 in/min. The hatch spacing was 0.0208 in. The top layer was then milled to a depth of cut of 0.003 in to achieve the desired part geometry and surface finish, with the spindle speed maintained at a constant 3000

rpm. The in-feed during milling was 0.04 in and feed rate 10 in/min. The hybrid cycle process parameters are listed in Table 1. It is to be noted that the milling in-feed is almost twice as that of hatch spacing during the printing cycle.

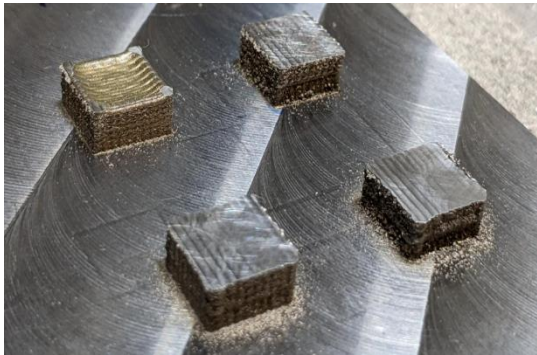


**Figure 2:** 3D printed SS316L samples

Additive (3D printing) cycle (Laser power = 250W)		In-situ finishing (milling) cycle (Tool diameter = 0.375 in)	
Hatch spacing	<b>0.0208 in</b>	In-feed	<b>0.04 in</b>
Scan speed	<b>10 in/min</b>	Feed rate	<b>10 in/min</b>
Layer thickness	<b>0.015 in</b>	Depth of cut	<b>0.003 in</b>
Powder flow rate	<b>4 rpm</b>	Spindle speed	<b>3000 rpm</b>

**Table 1:** Hybrid cycle process parameters

## 2.2. Data Synchronization of Multimodal Sensors

The multimodal data streams captured from various sensors are synchronized to less than about 1 millisecond accuracy for the complete duration of the experiments. Each voxel represents surface segments of dimension 0.042 x 0.040 in (1.05 x 1.02 mm) and encompasses 2 printing tracks **S\_T11** and **S\_T21** and 1 milling pass **S\_M11**. The voxelized surface along with the direction of each of the printing scans and milling passes are indicated in Figure 3. Signal data from all sensor channels are segmented in accordance with the voxelized surface structure, thus capturing both material and information flow at each voxel throughout the entire manufacturing process chain. Here, information based on time-frequency patterns from both accelerometer and AE data channels collected during the process chain are used to accurately predict the occurrence of surface porosity in each voxel. Both accelerometer and AE sensors are placed beneath the powder collection tray inside the DED hybrid machine. The sampling frequency of the accelerometer is 10,000 Hz while that of AE sensor is 100,000 Hz. The high sensitivity and temporal resolution of these sensors along with their low hardware cost makes it feasible to localize the occurrence of surface porosity in voxels.

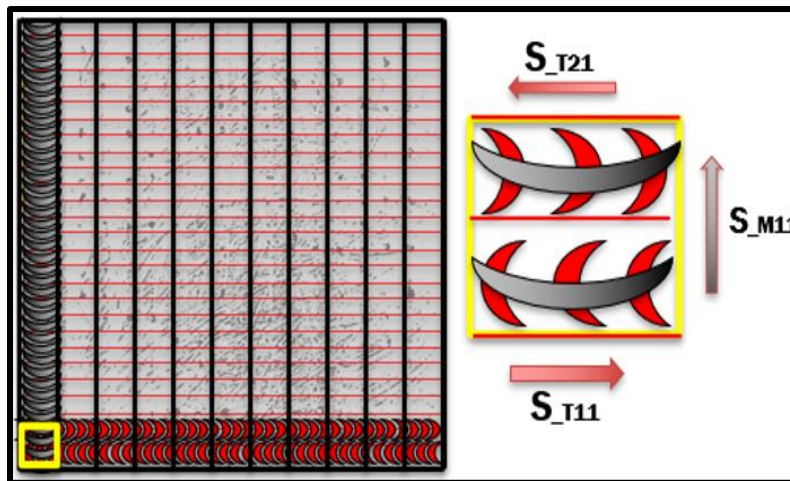


**Figure 3:** Graphical representation of printing and milling paths in the highlighted voxel at the top layer

### 2.3. Representation of Voxel-wise Porosity for Surface Images

Images of the top surface are captured using a digital camera after the milling cycle. These top view images are segmented into voxels whose dimensions are defined in Section 2.2. Post processing of the voxelized images into grayscale and subsequently into black and white is performed to characterize the ground truth porosity. A critical aspect of this process is the threshold setting of the pixel grayscale intensity with which the pixels are categorized as either black or white based on their grayscale value that ranges between 0 and 255. From this image dataset, we set the threshold value to 106 enabling us to capture the pores' geometry at its fullest in each of the voxels while avoiding the noise due to the presence of scratches on the part's surface.

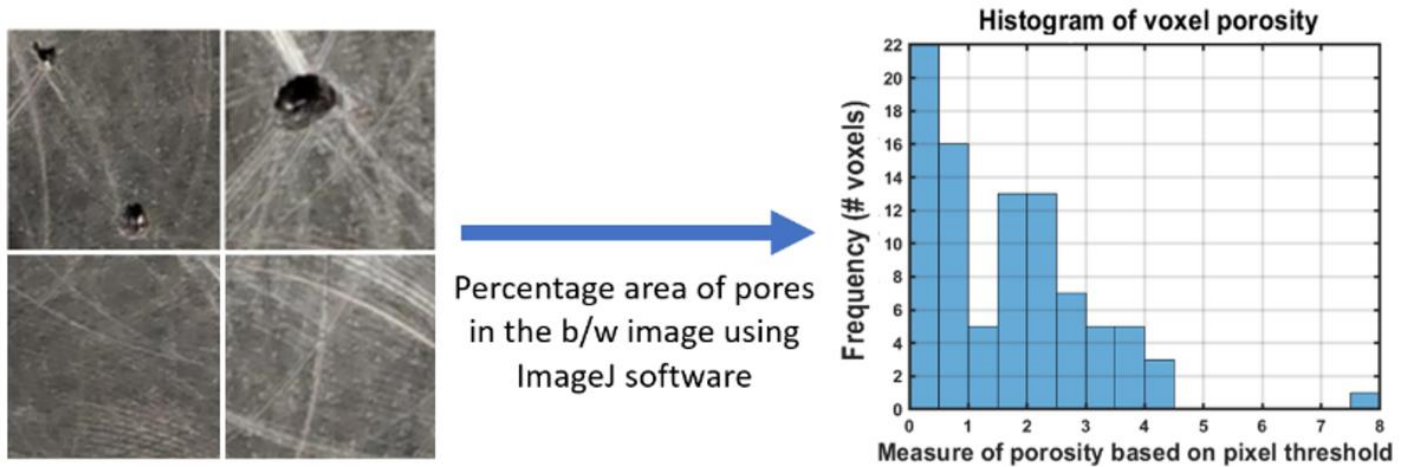


**Figure 4:** Images of porous and non-porous voxels in the top layer and the histogram of porosity measures (percentage area of pores) in voxels based on pixel thresholding using ImageJ software.

The percentage area of pores in each of the voxel images, obtained using ImageJ software is used as a measure of porosity, as illustrated by the histogram in Figure 4. We formulate a binary image classification model, wherein images of voxels having percentage area of pores less than 1% are classified as non-porous voxels, and those having percentage areas greater than 2% are considered porous voxels. The accelerometer and AE signal spectrograms for each voxel, pertaining to various stages of the process chain (printing and milling cycles) are stacked to form tensor inputs for our CNN models (Figure 6).

### 3. XAI AND LOCAL INTERPRETABLE MODEL-AGNOSTIC EXPLANATIONS (LIME)

Rapid advancements in computational power and sophisticated machine learning algorithms have led to significant developments in AI technologies over the last couple of decades. Deep learning models have demonstrated excellent capabilities in the manufacturing domain, particularly in real-time process monitoring and anomaly detection based on multimodal data fused from various sensors. They enable manufacturers to monitor their operations in real-time, identify issues that may arise, and make corrective actions resulting in significant cost savings. However, such deep learning models are highly non-linear in nature, and interpreting the model predictions to understand the effect of various features become cumbersome. Hence the true potential of such deep learning models can only be realized with good explainability. Without explainability, such models can result in incomprehensible false positives leading to incorrect

decision-making, additional costs and mistrust in these models. Therefore, in addition to achieving high prediction accuracies using complex ‘black box’ machine learning models, it becomes even more important to dissect as to why a particular model arrived at a specific outcome, even if it was the right inference, in order to gather deeper insights into the decision-making process of the ‘black box’ models.

Towards this pursuit, explainable AI (XAI) techniques are garnering significant interests and strive to make these ‘black box’ models more transparent, interpretable, and trustable by providing justifications for a particular output and why a particular decision was made. XAI techniques are generally classified into ante-hoc and post-hoc approaches [40]. Ante-hoc approaches use transparent models such as linear regression, decision trees, and modified neural networks making it easier to retrace the built-in decision process. In practice, they are adopted when the underlying relationships are simple and/or adequate domain expertise exists beforehand to determine useful features towards building accurate models [41]. However, ante-hoc approaches may not be suitable for more complex models involving high dimensional data, as they introduce bias into the explanation by focusing on specific features or assumptions made during the modeling process, leading to incomplete or inaccurate explanations of the model’s behavior. On the other hand, post-hoc methods such as LIME construct surrogates of pre-trained complex models giving rise to intuitive explanations and reasoning that the complex ‘black box’ models could not provide in the first place [31, 42]. LIME operates on the premise that the ‘black box’ models behave differently in different regions of the input space. Instead of providing a global explanation for the complex model across all possible inputs, LIME focuses on the model’s prediction for a specific instance or small neighborhood of instances in the input space, providing localized and interpretable explanations. LIME develops piece-wise linear approximations to effectively capture the behavior of the ‘black box’ model around the vicinity of inputs. Such local linear approximations can provide insights into the decision-making process of the ‘black box’ model at a granular level. It can reveal which features are most important for the ‘black box’ model’s decision for a particular input instance. This information can be used to reduce the biases associated with the model while boosting its performance by fine-tuning. By understanding what features are driving a model’s decision-making, manufacturers can make more informed decisions during operations. In Figure 5, the CNN architecture used for classifying the occurrence of defects in 3D printed parts using ultrasound images [16] is considered as an example of a

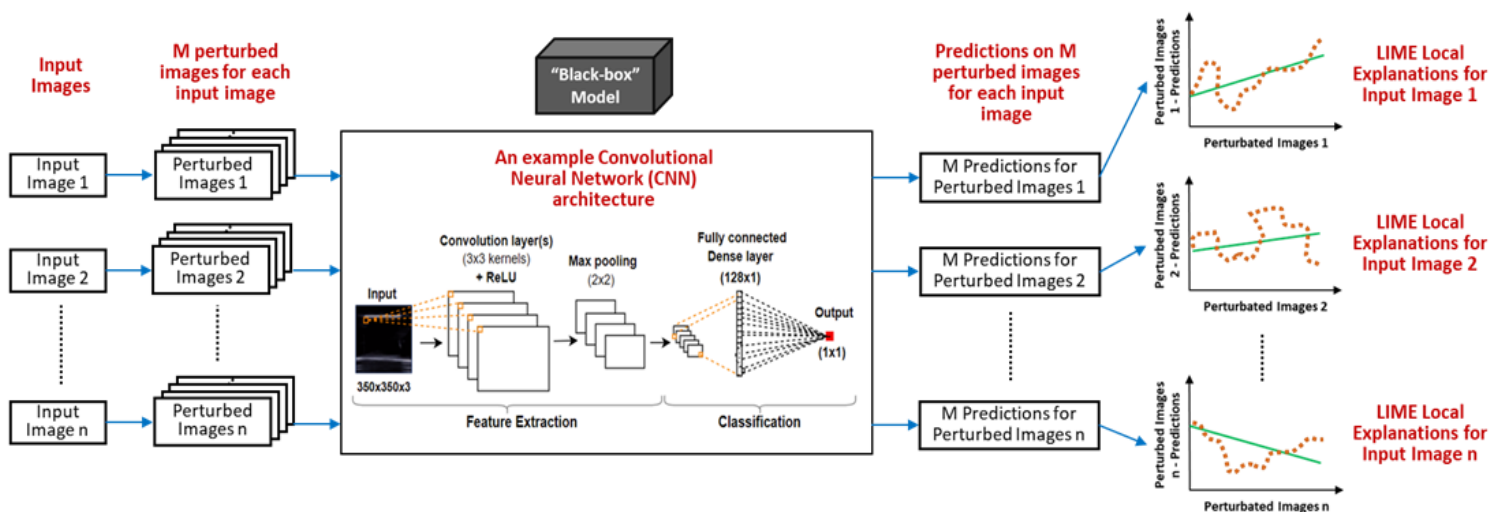


**Figure 5:** Graphical illustration explaining the intuition behind LIME for an ultrasound image-based internal defect detection problem on 3D printed parts

‘black box’ model. The plots on the right in Figure 5 represent the linear approximations (green) for the predictions on the perturbed dataset (orange) for various inputs. The ‘black box’ model can be locally approximated to this linear model wherein the coefficients represent the importance of each feature in the model’s decision-making process.

In this study, we extend the implementation of LIME to 3D tensors comprising signal spectrograms from multiple channels. We aim to identify significant frequency bands from each channel that correlate to the occurrence of porosity in localized surface segments. Instead of considering the complex functional relationship that CNN and other ‘black box’ models capture, LIME aims to explain the relationship local to the various neighborhoods of the input space (here, a neighborhood consists of signal spectrograms that are similar to each other). Synthetic perturbed image samples are generated within the neighborhood of a data channel to construct a highly interpretable linear model using these samples that will hold only for that neighborhood.

Mathematically, let us denote the CNN binary classifier model as a function  $f$ , which partitions the space of inputs constituting various “porous” and “non-porous” voxels into two regions. To get a local explanation about a tensor  $T$  in the input space, LIME first segments each channel  $x$  into  $d$  parts. Unlike an image where similar pixels can be grouped into segments of many sizes; each component of the spectrogram represents the energy captured over time and frequency, and are considered as individual elements. Since the model under consideration has input tensor with 4 signal spectrograms (channels) corresponding to the printing cycle,  $d$  equals 1935 which is  $129 \times 15$ . For every channel in this tensor, we construct a mask  $x' \in \{1\}^d$ , i.e., a binary vector where all the  $d$  elements are one. All the masks are concatenated to form a single unwrapped mask having  $N * d$  elements in total (refer Figure 6). Then, LIME creates  $M$  different perturbation masks  $z'_i \in \{1\}^{N*d}$  where  $(i = 1,2,3, \dots M)$ , by randomly setting some of the elements in  $x'$  to zero in each channel according to a Bernoulli distribution, i.e., Bernoulli(0.5). Each of these masks correspond to a perturbed image  $z_i$ ,  $(i = 1,2,3, \dots M)$  in the input space.

The CNN model  $f$  then makes predictions on all these images  $z_i$ . The output layer of our CNN model employs a sigmoid activation function, resulting in each prediction being a single probability towards the class that is encoded as one [43]. Each perturbed image  $z_i$  is weighted by an index  $\pi_x(z_i)$  based on how similar  $z_i$  is to  $x$ . This similarity index is defined using a radial basis kernel as follows:

$$\pi_x(z_i) = \exp\left(\frac{-D(x,z_i)^2}{\delta^2}\right) \quad (3.1)$$

where  $\delta$  is the kernel width. The similarity  $D(x, z_i)$  between  $x$  and  $z_i$  is calculated as the cosine of the angle between their vector masks  $x'$  and  $z'_i$ . LIME trains a linear model  $g$ , defined by its coefficient vector  $\beta^*$

$$\beta^* = \operatorname{argmin}_{\beta} \sum_{i=0}^M \pi_x(z_i) [f(z_i) - \langle \beta, z'_i \rangle]^2 + \lambda \langle \beta, \beta \rangle \quad (3.2)$$

where  $z_0 = x$ ,  $z'_0 = x'$ ,  $f(z_i)$  is the output of the CNN model and  $\lambda$  is the ridge regularization term that penalizes the linear model when its complexity increases. This trained linear model approximates the behavior of CNN model  $f$  in the vicinity of the original input. The sign and magnitude of each element of  $\beta^*$  indicate positive or negative importance of the presence of corresponding segment in  $z$ . In addition, a total of  $2^d - 1$  possible perturbations exist to estimate  $\beta^*$  about every perturbed spectrum  $z$ . Employing all possible permutations become computationally intractable. Hence, a smaller value of  $M$  is chosen based on the following theorem.

**Theorem 1.** (Perturbed sample size) [42]: The number of perturbed instances  $M$ , required to achieve an uncertainty interval width  $w$  of feature importance at a user-specified confidence level  $\alpha$  can be estimated as follows:

$$M = \frac{4\varepsilon^2}{\bar{\pi} * \left[ \frac{w}{\phi^{-1}(\alpha)} \right]^2} \quad (3.3)$$

where  $\bar{\pi}$  is the average weight estimated from an initial set of  $J$  perturbed instances as  $\bar{\pi}_J = \sum_{i=0}^J \pi_x(z_i) / J$ ,  $\varepsilon^2$  is the empirical sum of squared errors between a LIME model and  $g$ , weighted by  $\pi_x(z_i)$  for  $i = 1, 2, 3, \dots, J$  and  $\phi^{-1}(\alpha)$  is the two-tailed inverse normal cumulative distribution function at confidence level  $\alpha$ .

The above theorem serves as a guiding framework towards balancing the trade-off between the number of perturbations required and the uncertainty associated with the explanations. The number of perturbed instances  $M$  has to be sufficiently large to keep the uncertainty width  $w$  small. A high degree of perturbation can lead to a more accurate approximation of the ‘black box’ model but may also make the explanation less interpretable. On the other hand, a low degree of perturbation may result in a more interpretable explanation but could be less accurate. One of the challenges associated with LIME is the need to consolidate local explanations and derive a global explanation consistent across the input space. Energy contained in frequency bands that are considered important for some porous voxels may not be that important for other porous voxels. Such inconsistencies in explanations may arise due to the following factors: (i) The explanations from the local linear models are based on a subset of all possible input perturbations generated at random. Therefore, a different set of perturbations could yield a different explanation altogether. (ii) It is possible for the linear models to not capture the high non-linearity prevalent in certain local input neighborhoods. This essentially translates to the local linear model underfitting the behavior of ‘black box’ model in the region of concern. Therefore, in order to achieve consistent global explanations, LIME explanations need to be considered only when the linear model is faithful enough to the ‘black box’ model locally. The accuracy of the linear model  $g$  should be high as it tries to map the perturbed images  $z_i$  to  $f(z_i) \in (0,1)$ . By implementing uniform segmentation across different channel frequency bands and considering LIME explanations only from instances that have a  $R^2$  value of greater than 0.75, we derive a measure of global importance for energy contained in frequency bands from different channels that can explain the occurrence of surface porosity in voxels.

#### 4. RESULTS

Our dataset consists of 72 voxels from the top layer, where each voxel encompasses 2 printing tracks and 1 milling pass. Each signal spectrogram has a dimension of 129 x 15, capturing the energies of 129 frequency bands across 15-time instances pertaining to that voxel. It is important to note that the frequency bandwidths captured in the respective signal spectrograms will be proportional to their sampling frequency. Three models were developed using input data captured at various stages of the process chain. The input for all the models is a tensor of dimension  $N \times 129 \times 15$ , where  $N$  represents the number of data channels as described in Table 2. The first model uses spectrograms from accelerometer and AE signals captured during the printing cycles. In this case, the input tensor for each voxel has a dimension of 4 x 129 x 15, with the two sensors capturing data for both the printing tracks. The second model is developed using spectrograms captured during the milling cycle alone. Here, the input tensor for each voxel has a dimension 2 x 129 x 15.

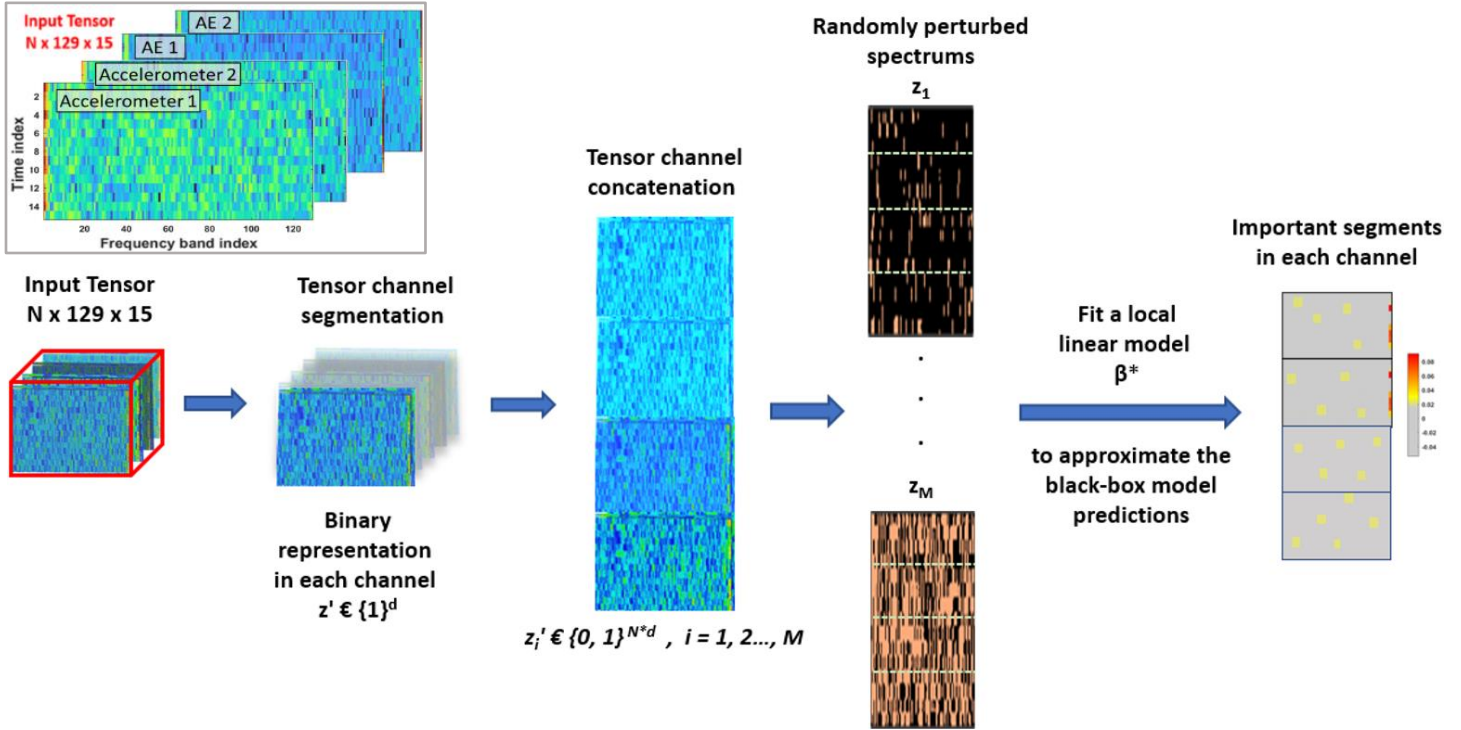


**Figure 6:** An illustration of the LIME scheme with input features (spectrograms) stacked as a tensor.

The third model uses signal spectrograms from both printing and milling cycles, resulting in an input tensor dimension of  $6 \times 129 \times 15$ . A  $k$ -fold cross validation is performed for each of the above models to establish better generalization. The entire dataset is randomly split into training and testing in the ratio 8:1. Employing an 8-fold cross validation on the training set ensures an equal number of data samples between the validation and test sets. This essentially translates to 56 voxels for training and 8 voxels each for validation and testing purposes. The CNN architecture for all the models, as shown in Figure 7 comprised of two convolution layers having 6 and 1 filters respectively, each followed by a max pooling layer, and finally a fully connected dense layer with 6 neurons. Rectified Linear Unit (ReLU) activation function was employed after each of the convolutional layers. The output layer was followed by the sigmoid activation function. A stochastic gradient-descent optimizer with a learning rate of 0.001 was used to minimize loss and a binary cross entropy quantifier was used to measure the accuracy.

Information based on signal data from printing cycles is found to be most sensitive to capture surface porosity in voxels, as seen from the box plots indicating training, validation and testing accuracies of the 8-fold cross validation models in Figure 8. The median validation and testing accuracies significantly increase in the presence of data from printing cycles. The prediction accuracies obtained in case (a) and (c) are statistically the same. The small variations in the validation and testing accuracies in the box plots pertaining to cases (a) and (c) can be attributed to the small dataset being used in this study. The best models (folds) for both cases (a) and (c) have training and validation accuracies of 100% and 75% (translating to 6 out of 8 correct classifications) and testing accuracies of 75% and 87.5% (translating to 7 out of 8 correct classifications) respectively. The confusion matrices in Table 3 indicate the performance of the best classification model (fold) for each case (a), (b) and (c). In the next part, we analyze the inferences from LIME for the best model with input data pertaining to printing cycles.

Number of data channels (N)	CNN Model (Input features)
4	Printing cycles only
2	Milling cycle only
6	Both printing and milling cycles combined

**Table 2:** Size of input data channels pertaining to each developed CNN model

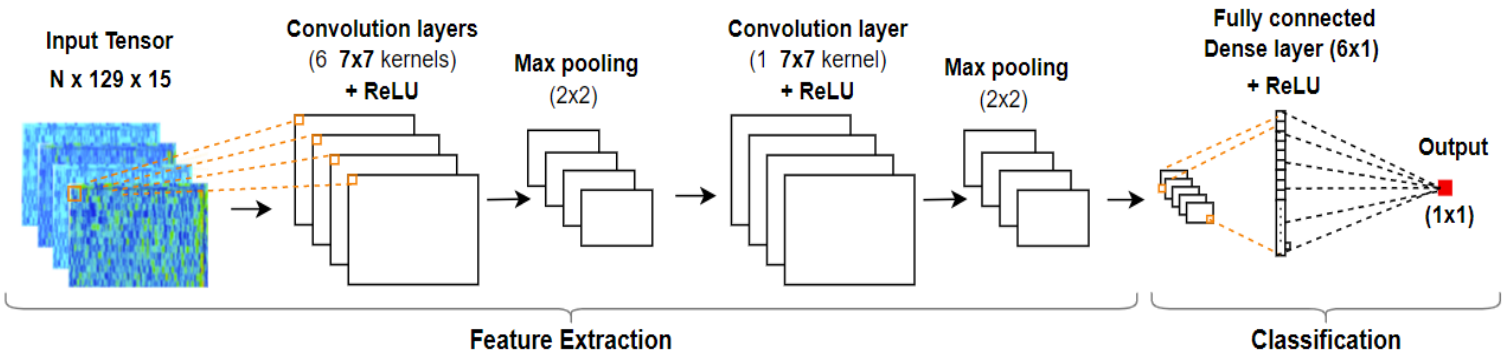


**Figure 7:** The CNN architecture employed for predicting voxels with porosity using accelerometer and AE signal spectrograms integrated into a tensor

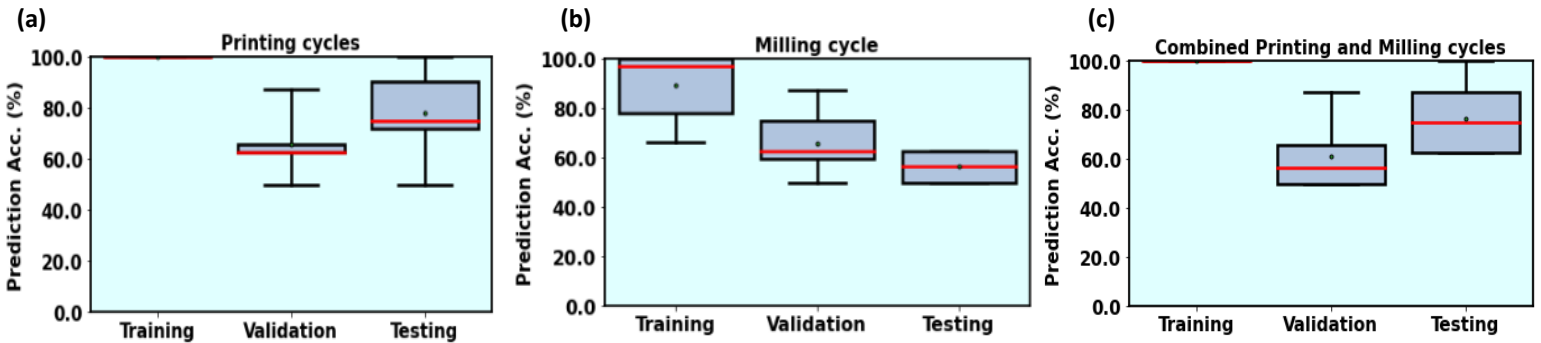


**Figure 8:** Box plot summary of prediction accuracies for training, validation and testing datasets over the 8-fold cross validation models using signal spectrograms from (a) only printing cycles (b) only milling cycle (c) both printing and milling cycles combined.

Dataset	Process chain Prediction class	(a) Printing cycle		(b) Milling cycle		(c) Combined cycle	
		Porous	Non-porous	Porous	Non-porous	Porous	Non-porous
Training	Porous	31	0	28	0	27	0
	Non-porous	0	25	0	28	0	29
Validation	Porous	3	0	3	2	4	0
	Non-porous	2	3	0	3	1	3
Testing	Porous	5	0	3	3	1	1
	Non-porous	1	2	0	2	1	4

**Table 3:** Confusion matrices indicating the performance of best classification model (fold) in each case using signal spectrograms from (a) only printing cycles (b) only milling cycle (c) both printing and milling cycles combined.

#### 4.1. XAI-derived AE features

We now consider 6 correctly classified porous voxels and 6 correctly classified non-porous voxels with high explanation scores. LIME signifies components in the highest frequency band of AE spectrogram pertaining to both printing tracks to be most important towards correct classification of surface porosity for all voxels (refer Figure 9).

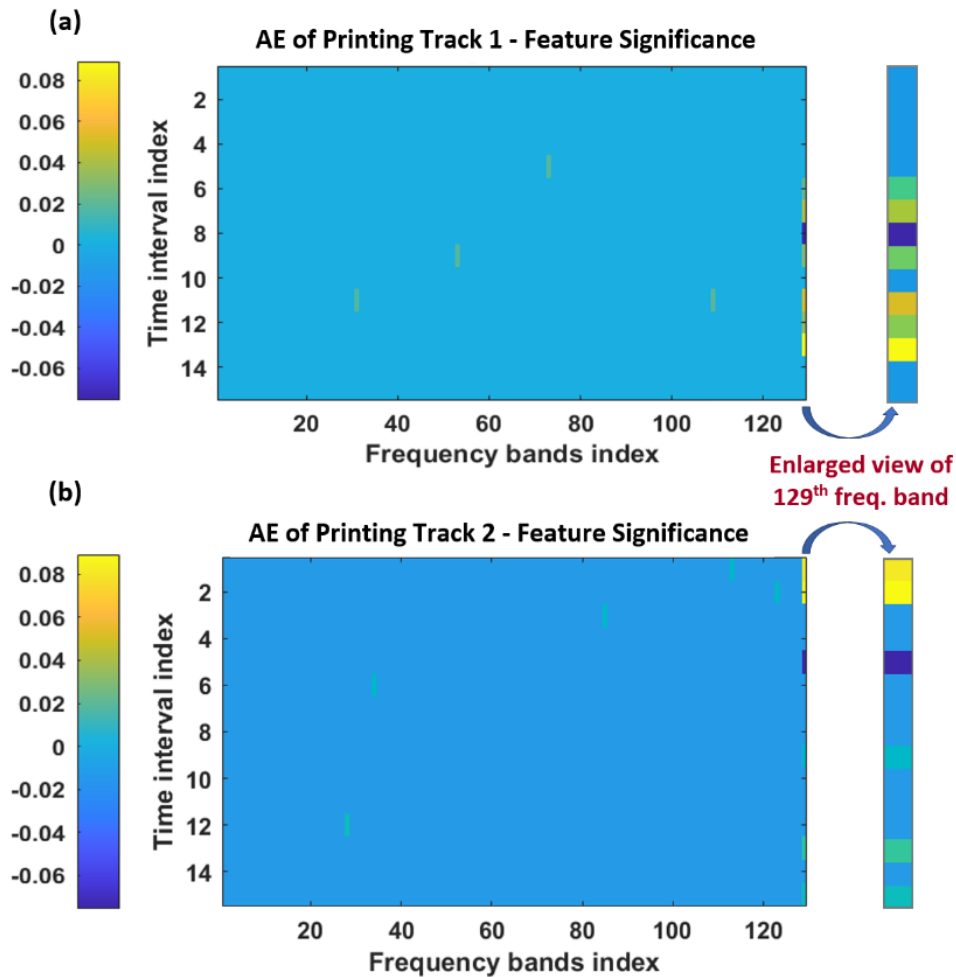


**Figure 9: (a,b)** Significance of super pixels in AE spectrograms based on LIME analysis for each printing track (P1 and P2) contained in a correctly classified porous voxel.

The color bar in both the plots indicate the significance of the super pixel contributing towards the classification model decision. This band translates to **49612 – 50000 Hz** frequency range of the AE spectrum. The relative importance of other frequency bands in both accelerometer and AE spectrograms are low by an order of magnitude and differ from voxel to voxel. Among the 6 porous voxels, 4 are considered to have high likelihood of pore formation due to inefficient overlapping between adjacent tracks and the remaining 2 voxels are considered to have high likelihood of pore formation due to spatter events. This classification amongst the porous voxels is made based on the shapes, sizes and location of pores observed from the images. Pore formation associated with spatter events in DED are predominantly characterized with the occurrence of small round pores/voids in the center region of printing tracks [14]. Since each voxel contains two printing tracks, we associate pores formed due to inefficient overlapping to be present between the tracks in the center region of the voxel and pores formed due to spatter events to be scattered on the sides of the voxel. The median

peak energy values contained in high frequency AE band are observed to be **18.54 db/Hz** for voxels with pore formation due to insufficient fusion between adjacent printing tracks, **23.61 db/Hz** for voxels with high likelihood of pore formation due to spatter events and **28.84 db/Hz** for non-porous voxels, as shown in Figure 10. The relatively higher peak energy values observed for non-porous voxels in the 49612-50000 Hz frequency band of AE spectrum is a consequence of increased laser-material interaction in the melt pool, compared in contrast to other voxels with pore formation due to spatter events and ineffective overlap between adjacent printing tracks from low heat input.

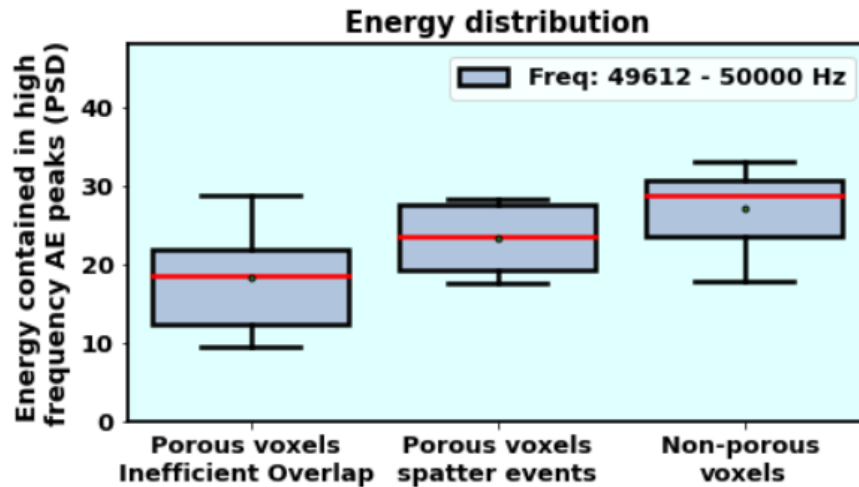


**Figure 10:** Box plots indicating the variation in median peak energies contained in high frequency AE band (#129) for porous voxels attributed to two mechanisms of pore formations, and non-porous voxels.

LIME also indicates positive significance (between 0.01 to 0.03) for few constituents in the 30th to 36th frequency bands translating to **11000 - 14000 Hz** for porous voxels due to inefficient overlap (refer Figure 9). However, the energy contained in the low frequency bands are observed to be an order of magnitude lower than the energy contained in the 129<sup>th</sup> frequency band. Similar trends in power spectral density of AE signals have been reported by Pandian *et al.* in [44] corresponding to lack of fusion, no pores and keyhole defects in LPBF process for SS316L. The above inferences are based on analyzing the individual constituents of spectrograms that have high significance as indicated by LIME. Each of the 4 spectrograms of the input tensor comprises 1935 constituents (i.e., 129 x 15), thereby resulting in a total of 7740 spectrogram constituents for each voxel. The first two spectrograms correspond to accelerometer data and the last two spectrograms correspond to AE data for both the printing tracks. All constituents that have either positive or negative significance value of greater than 0.05 are found to occur in the 129<sup>th</sup> frequency band of AE spectrograms translating to 49612 – 50000 Hz frequency range (refer Figure 11). 58xx (indices between 5790 and 5805) and 77xx (indices between 7725 and 7740) represent the 129<sup>th</sup> frequency band constituents of AE data from the first and second printing tracks respectively in each voxel. The high energy constituents of the 129<sup>th</sup> frequency band are found to have positive significance (> 0.08) for porous voxels and negative significance (< - 0.05) for non-porous voxels, as shown in Figure 12. A closer look at the constituents of this high frequency band together with the thermal sensor data reveals a correlation between the high energy constituents and the occurrence of spatter events from melt pool images. These findings can pave way for the energy contained in the high frequency AE spectrogram components to capture the occurrence of spatter events in voxels that result in surface porosity during the printing cycles.

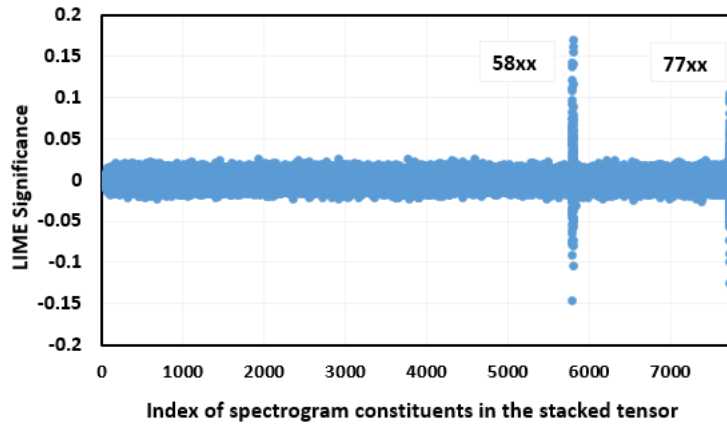


**Figure 11:** LIME significance of spectrogram constituents contained in the 6 porous and 6 non-porous voxels under consideration

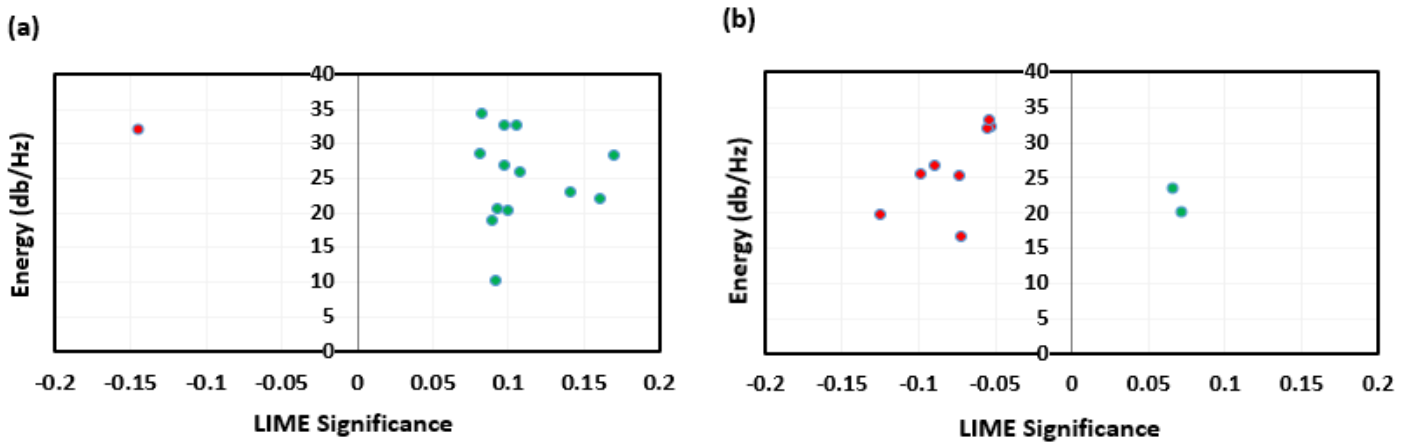


**Figure 12:** AE Spectrogram constituents in the 129<sup>th</sup> frequency band with LIME significance magnitude greater than 0.05 and their corresponding energy distribution for (a) 6 porous and (b) 6 non-porous voxels under consideration

#### 4.2. Inferences via Thermal Imaging-AE Sensor Fusion

The occurrence of spatter events is observed in all voxels during DED with the help of ThermaViz melt pool sensor. The thermal images of the melt pool are continuously captured at a frequency slightly greater than half of that of high frequency components in the AE spectrogram. An average of 7.9 melt pool frames is acquired for each printing track within a voxel, corresponding to 15 spectrogram constituents of the high frequency AE band. This translates to approximately 2 constituents of the AE 129<sup>th</sup> frequency band being captured per melt pool frame of the thermal sensor. The energy contained in the high frequency AE band spectrogram constituents are found to have an oscillatory pattern along the printing track. Figure 13 depicts the energy contained in high frequency AE band spectrogram constituents during a printing cycle passing through 4 voxels that are sequentially located. Non-porous voxels are found to have slightly higher peak energies in the 49612-50000 Hz frequency band compared to porous voxels. The melt pool thermograms pertaining to the peak indices (namely B, D, F, H, J, L and N) indicate the presence of spatter events and the valley indices (namely A, C, E, G, I, K and M) indicate the absence of spatter events, as shown in Table 4. To further verify this correlation between the energy contained in high-frequency AE band and the spatter events captured in melt

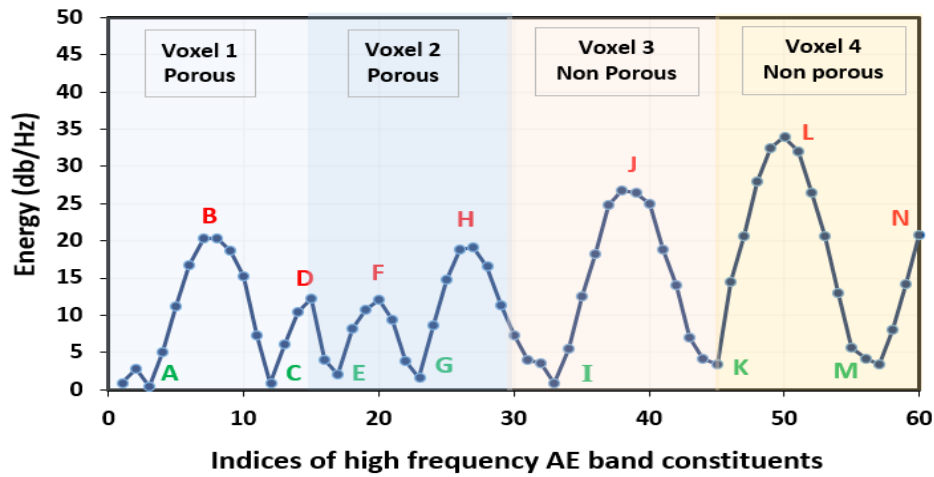


**Figure 13:** Oscillatory patterns observed in the energy values of AE signal spectrogram constituents in the high frequency (129<sup>th</sup>) band within a printing track containing porous and non-porous voxels

pool thermograms, a total of 4 complete printing tracks were considered for evaluation. In the 46 peaks (crests) observed in the energy values contained in high frequency AE band, the presence of spatter events was identified in 41 instances. These spatter events were mostly accompanied by high peak temperatures in the melt pool. There were 2 instances of false positives when AE energy was high and no spatter particles or events were observed in the thermograms, which could be due to AE sensor capturing elastic waves from the laser beam or table motion system. Similarly, in the 49 occasions of valley points (troughs) observed, 32 instances had thermograms devoid of spatters. 9 instances were classified as indeterminate due to the absence of spatter particles and presence of mild disturbances in the thermograms mainly attributed to irregular reflections during the melt pool capture. The above findings are consolidated into a confusion matrix in Table 5. The median energy contained in the peaks is **26.73 db/Hz** while that of valleys is **2.62 db/Hz** as highlighted in Figure 14.

Sensor Fusion (AE / Thermal)	Spatter events	No spatter observed	Indeterminate
Peaks (46)	41	2	3
Valleys (49)	8	32	9

**Table 5:** Confusion matrix highlighting the correlation between energy contained in high frequency AE spectrogram band and spatter events in melt pool thermograms.

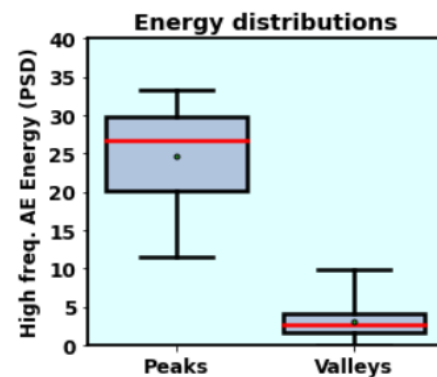


**Figure 14:** Box plots indicating the differences in energy contained in peaks and valleys of high frequency AE band (#129) across the 4 printing tracks under consideration

INDEX	THERMOGRAM	INDEX	THERMOGRAM	VOXELIZED IMAGES ALONG THE TRACK
<b>A</b>		<b>B</b>		<p><b>Voxel 1</b></p> <p>Signatures in spatter events resulting in pores in printing tracks contained in voxels 1 and 2 with low peak energies in high frequency AE band.</p>
<b>C</b>		<b>D</b>		
<b>E</b>		<b>F</b>		<p><b>Voxel 2</b></p>
<b>G</b>		<b>H</b>		
<b>I</b>		<b>J</b>		<p><b>Voxel 3</b></p> <p>Spatter events in non-porous voxels 3 and 4 with high peak energies in high frequency AE band owing to stronger laser material interaction.</p>
<b>K</b>		<b>L</b>		
<b>M</b>		<b>N</b>		<p><b>Voxel 4</b></p>

**Table 4:** Thermograms indicating the presence and absence of spatter events corresponding to peaks and valleys of energy contained in the high frequency AE band, as observed in Figure 13.

The correlation between energy contained in the high-frequency AE band and spatter events captured in the melt pool thermograms could be realized because of our robust multimodal sensor data synchronization and alignment at the voxel level with 0.1 millisecond temporal resolution and 0.5 millimeter spatial resolution. Given the low laser power (250W) employed in this study, we find spatter events that result in surface porosity in voxels to have lesser peak energy values in the high frequency AE band compared to those resulting in non-porous voxels. The high sensitivity and temporal resolution offered by AE sensors coupled with its cost effectiveness can be tapped to great use for real time in-situ monitoring of laser-material interactions in DED processes. The findings presented here further opens avenues to understand the signatures in time-frequency patterns of AE signal pertaining to the occurrence of spatter events resulting in localized defects such as porosity and their underlying formation mechanisms for different process parameters including laser power, scan speed and powder feed rate.

## 5. CONCLUSION

This study has helped us identify important features in AE signal spectrograms captured during the printing cycles that significantly contribute towards the correct classification of porous voxels in additively manufactured SS316L parts.

- As part of our smart hybrid manufacturing implementation, multimodal sensor signals captured during the entire process chain were synchronized to within 0.1 millisecond accuracy and aligned with 0.5 millimeter spatial resolution. The process of voxelization helps capture material and information flow at each voxel in the entire manufacturing process chain.
- Having developed multiple classification machine learning models using voxelized sensor data from printing and milling cycles, we found signal data from printing cycles to be most sensitive in capturing surface porosity in voxels achieving a prediction test accuracy of over 87%.
- With the help of explainable AI, we were able to identify differences in peak energy values contained in the high frequency AE band pertaining to the two modes of pore formation observed due to spatter events in DED and incomplete fusion between adjacent printing tracks from low heat input. Non-porous voxels were found to have higher peak energy values in the high frequency AE band compared to other porous voxels owing to the strong laser-material interaction in the melt pool.
- The robust multimodal sensor data alignment helped identify the underlying correlation between energy contained in high frequency bands of AE spectrogram and the occurrence of spatter events in melt pool images from the thermal sensor. This serves as evidence for AE signals to capture the occurrence of spatter events and opens future opportunities to investigate the time-frequency patterns of AE signal towards characterizing laser-material interactions and different spatter event mechanisms as described by authors in [21].

## References

- [1] Z. Doubrovski, J. C. Verlinden, and J. M. Geraedts, "Optimal design for additive manufacturing: opportunities and challenges," in *International design engineering technical conferences and computers and information in engineering conference*, 2011, vol. 54860, pp. 635-646.

- [2] N. Guo and M. C. Leu, "Additive manufacturing: technology, applications and research needs," *Frontiers of mechanical engineering*, vol. 8, no. 3, pp. 215-243, 2013.
- [3] A. Dass and A. Moridi, "State of the art in directed energy deposition: From additive manufacturing to materials design," *Coatings*, vol. 9, no. 7, p. 418, 2019.
- [4] M. Borish, B. K. Post, A. Roschli, P. C. Chesser, and L. J. Love, "Real-time defect correction in large-scale polymer additive manufacturing via thermal imaging and laser profilometer," *Procedia Manufacturing*, vol. 48, pp. 625-633, 2020.
- [5] M. Liu, A. Kumar, S. Bukkapatnam, and M. Kuttolamadom, "A review of the anomalies in directed energy deposition (DED) Processes & Potential Solutions-part quality & defects," *Procedia Manufacturing*, vol. 53, pp. 507-518, 2021.
- [6] A. Mostafaei, C. Zhao, Y. He, S. R. Ghiaasiaan, B. Shi, S. Shao, N. Shamsaei, Z. Wu, N. Kouraytem, and T. Sun, "Defects and anomalies in powder bed fusion metal additive manufacturing," *Current Opinion in Solid State and Materials Science*, vol. 26, no. 2, p. 100974, 2022.
- [7] A. Y. Al-Maharma, S. P. Patil, and B. Markert, "Effects of porosity on the mechanical properties of additively manufactured components: A critical review," *Materials Research Express*, vol. 7, no. 12, p. 122001, 2020.
- [8] A. Matsunawa, M. Mizutani, S. Katayama, and N. Seto, "Porosity formation mechanism and its prevention in laser welding," *Welding international*, vol. 17, no. 6, pp. 431-437, 2003.
- [9] Z. Ren, L. Gao, S. J. Clark, K. Fezzaa, P. Shevchenko, A. Choi, W. Everhart, A. D. Rollett, L. Chen, and T. Sun, "Machine learning–aided real-time detection of keyhole pore generation in laser powder bed fusion," *Science*, vol. 379, no. 6627, pp. 89-94, 2023.
- [10] A. Sola and A. Nouri, "Microstructural porosity in additive manufacturing: The formation and detection of pores in metal parts fabricated by powder bed fusion," *Journal of Advanced Manufacturing and Processing*, vol. 1, no. 3, p. e10021, 2019.
- [11] D. Gu, Y. Hagedorn, W. Meiners, G. Meng, and R. Batista, "S.; Wissenbach, K.; Poprawe, R. Densification behavior, microstructure evolution, and wear performance of selective laser melting processed commercially pure titanium," *Acta Mater*, vol. 60, pp. 3849-3860, 2012.
- [12] S. A. Khairallah, A. T. Anderson, A. Rubenchik, and W. E. King, "Laser powder-bed fusion additive manufacturing: Physics of complex melt flow and formation mechanisms of pores, spatter, and denudation zones," *Acta Materialia*, vol. 108, pp. 36-45, 2016.
- [13] J. Huang, M. Li, J. Wang, Z. Pei, P. McIntyre, and C. Ma, "Selective laser melting of tungsten: Effects of hatch distance and point distance on pore formation," *Journal of Manufacturing Processes*, vol. 61, pp. 296-302, 2021.
- [14] J. H. L. Pang, J. Kaminski, and H. Pepin, "Characterisation of porosity, density, and microstructure of directed energy deposited stainless steel AISI 316L," *Additive Manufacturing*, vol. 25, pp. 286-296, 2019.
- [15] M. Khanzadeh, S. Chowdhury, M. A. Tschopp, H. R. Doude, M. Marufuzzaman, and L. Bian, "In-situ monitoring of melt pool images for porosity prediction in directed energy deposition processes," *IISE Transactions*, vol. 51, no. 5, pp. 437-455, 2019.
- [16] A. Karthikeyan, A. Tiwari, Y. Zhong, and S. T. Bukkapatnam, "Explainable AI-infused ultrasonic inspection for internal defect detection," *CIRP Annals*, 2022.
- [17] C. Zhao, K. Fezzaa, R. W. Cunningham, H. Wen, F. De Carlo, L. Chen, A. D. Rollett, and T. Sun, "Real-time monitoring of laser powder bed fusion process using high-speed X-ray imaging and diffraction," *Scientific reports*, vol. 7, no. 1, pp. 1-11, 2017.

- [18] C. L. A. Leung, S. Marussi, R. C. Atwood, M. Towrie, P. J. Withers, and P. D. Lee, "In situ X-ray imaging of defect and molten pool dynamics in laser additive manufacturing," *Nature communications*, vol. 9, no. 1, pp. 1-9, 2018.
- [19] S. J. Wolff, H. Wang, B. Gould, N. Parab, Z. Wu, C. Zhao, A. Greco, and T. Sun, "In situ X-ray imaging of pore formation mechanisms and dynamics in laser powder-blown directed energy deposition additive manufacturing," *International Journal of Machine Tools and Manufacture*, vol. 166, p. 103743, 2021.
- [20] S. J. Wolff, S. Webster, N. D. Parab, B. Aronson, B. Gould, A. Greco, and T. Sun, "In-situ observations of directed energy deposition additive manufacturing using high-speed x-ray imaging," *Jom*, vol. 73, no. 1, pp. 189-200, 2021.
- [21] Z. A. Young, Q. Guo, N. D. Parab, C. Zhao, M. Qu, L. I. Escano, K. Fezzaa, W. Everhart, T. Sun, and L. Chen, "Types of spatter and their features and formation mechanisms in laser powder bed fusion additive manufacturing process," *Additive Manufacturing*, vol. 36, p. 101438, 2020.
- [22] S. Ho, W. Zhang, W. Young, M. Buchholz, S. Al Jufout, K. Dajani, L. Bian, and M. Mozumdar, "DLAM: Deep Learning Based Real-Time Porosity Prediction for Additive Manufacturing Using Thermal Images of the Melt Pool," *IEEE Access*, vol. 9, pp. 115100-115114, 2021.
- [23] M. Khanzadeh, S. Chowdhury, M. Marufuzzaman, M. A. Tschopp, and L. Bian, "Porosity prediction: Supervised-learning of thermal history for direct laser deposition," *Journal of manufacturing systems*, vol. 47, pp. 69-82, 2018.
- [24] B. Zhang, S. Liu, and Y. C. Shin, "In-Process monitoring of porosity during laser additive manufacturing process," *Additive Manufacturing*, vol. 28, pp. 497-505, 2019.
- [25] M. Tang, P. C. Pistorius, and J. L. Beuth, "Prediction of lack-of-fusion porosity for powder bed fusion," *Additive Manufacturing*, vol. 14, pp. 39-48, 2017.
- [26] S. Shevchik, C. Kenel, C. Leinenbach, and K. Wasmer, "Acoustic emission for in situ quality monitoring in additive manufacturing using spectral convolutional neural networks.," *Additive Manufacturing*, vol. 21, pp. 598-604, 2018.
- [27] H. Gaja and F. Liou, "Defect classification of laser metal deposition using logistic regression and artificial neural networks for pattern recognition," *The International Journal of Advanced Manufacturing Technology*, vol. 94, no. 1, pp. 315-326, 2018.
- [28] H. Taheri, L. W. Koester, T. A. Bigelow, E. J. Faierson, and L. J. Bond, "In situ additive manufacturing process monitoring with an acoustic technique: clustering performance evaluation using K-means algorithm," *Journal of Manufacturing Science and Engineering*, vol. 141, no. 4, 2019.
- [29] K. Ito, M. Kusano, M. Demura, and M. Watanabe, "Detection and location of microdefects during selective laser melting by wireless acoustic emission measurement," *Additive Manufacturing*, vol. 40, p. 101915, 2021.
- [30] D. Gauder, M. Biehler, J. Gözl, V. Schulze, and G. Lanza, "In-process acoustic pore detection in milling using deep learning," *CIRP Journal of Manufacturing Science and Technology*, vol. 37, pp. 125-133, 2022.
- [31] M. T. Ribeiro, S. Singh, and C. Guestrin, "" Why should i trust you?" Explaining the predictions of any classifier," in *Proceedings of the 22nd ACM SIGKDD international conference on knowledge discovery and data mining*, 2016, pp. 1135-1144.
- [32] Y. Zhong, A. Tiwari, H. Yamaguchi, A. Lakhtakia, and S. T. Bukkapatnam, "Identifying the influence of surface texture waveforms on colors of polished surfaces using an explainable AI approach," *IISE Transactions*, pp. 1-15, 2022.
- [33] R. Y. Zhong, X. Xu, E. Klotz, and S. T. Newman, "Intelligent manufacturing in the context of industry 4.0: a review," *Engineering*, vol. 3, no. 5, pp. 616-630, 2017.

- [34] S. Catalucci, A. Thompson, S. Piano, D. T. Branson, and R. Leach, "Optical metrology for digital manufacturing: A review," *The International Journal of Advanced Manufacturing Technology*, pp. 1-20, 2022.
- [35] N. Ghosh, Y. Ravi, A. Patra, S. Mukhopadhyay, S. Paul, A. Mohanty, and A. Chattopadhyay, "Estimation of tool wear during CNC milling using neural network-based sensor fusion," *Mechanical Systems and Signal Processing*, vol. 21, no. 1, pp. 466-479, 2007.
- [36] M. Kumar and D. P. Garg, "Intelligent multi-sensor fusion techniques in flexible manufacturing workcells," in *Proceedings of the 2004 American Control Conference, 2004*, vol. 6: IEEE, pp. 5375-5380.
- [37] A. S. Iquebal, S. Pandagare, and S. Bukkapatnam, "Learning acoustic emission signatures from a nanoindentation-based lithography process: Towards rapid microstructure characterization," *Tribology International*, vol. 143, p. 106074, 2020.
- [38] A. S. Iquebal, B. Botcha, and S. Bukkapatnam, "Towards rapid, in situ characterization for materials-on-demand manufacturing," *Manufacturing Letters*, vol. 23, pp. 29-33, 2020.
- [39] B. Botcha, A. S. Iquebal, and S. T. Bukkapatnam, "Smart manufacturing multiplex," *Manufacturing Letters*, vol. 25, pp. 102-106, 2020.
- [40] W. J. Murdoch, C. Singh, K. Kumbier, R. Abbasi-Asl, and B. Yu, "Definitions, methods, and applications in interpretable machine learning," *Proceedings of the National Academy of Sciences*, vol. 116, no. 44, pp. 22071-22080, 2019.
- [41] O. Li, H. Liu, C. Chen, and C. Rudin, "Deep learning for case-based reasoning through prototypes: A neural network that explains its predictions," in *Proceedings of the AAAI Conference on Artificial Intelligence, 2018*, vol. 32, no. 1.
- [42] D. Slack, A. Hilgard, S. Singh, and H. Lakkaraju, "Reliable post hoc explanations: Modeling uncertainty in explainability," *Advances in Neural Information Processing Systems*, vol. 34, pp. 9391-9404, 2021.
- [43] I. Goodfellow, Y. Bengio, and A. Courville, "Deep Learning, ser. The Adaptive Computation and Machine Learning Series," ed: Cambridge, MA: The MIT Press, 2016.
- [44] V. Pandiyan, R. Drissi-Daoudi, S. Shevchik, G. Masinelli, R. Logé, and K. Wasmer, "Analysis of time, frequency and time-frequency domain features from acoustic emissions during Laser Powder-Bed fusion process," *Procedia CIRP*, vol. 94, pp. 392-397, 2020.
- [45] Q. Tian, S. Guo, E. Melder, L. Bian, and W. Guo, "Deep learning-based data fusion method for in situ porosity detection in laser-based additive manufacturing," *Journal of Manufacturing Science and Engineering*, vol. 143, no. 4, 2021.
- [46] A.-I. García-Moreno, J.-M. Alvarado-Orozco, J. Ibarra-Medina, and E. Martínez-Franco, "Image-based porosity classification in Al-alloys by laser metal deposition using random forests," *The International Journal of Advanced Manufacturing Technology*, vol. 110, no. 9, pp. 2827-2845, 2020.
- [47] A.-I. García-Moreno, "Automatic quantification of porosity using an intelligent classifier," *The International Journal of Advanced Manufacturing Technology*, vol. 105, no. 5, pp. 1883-1899, 2019.
- [48] G. Tapia, A. H. Elwany, and H. Sang, "Prediction of porosity in metal-based additive manufacturing using spatial Gaussian process models," *Additive Manufacturing*, vol. 12, pp. 282-290, 2016.
- [49] M. Aminzadeh and T. R. Kurfess, "Online quality inspection using Bayesian classification in powder-bed additive manufacturing from high-resolution visual camera images," *Journal of Intelligent Manufacturing*, vol. 30, no. 6, pp. 2505-2523, 2019.
- [50] S. Coeck, M. Bisht, J. Plas, and F. Verbist, "Prediction of lack of fusion porosity in selective laser melting based on melt pool monitoring data," *Additive Manufacturing*, vol. 25, pp. 347-356, 2019.

## APPENDIX

**Table 1A:** Summary of various machine learning based approaches used for the prediction of surface porosity in additive manufacturing.

Machine Learning algorithm	AM Process	Material type	Defect type	Ground Truth	Dataset type	Features	Accuracy
Clustering via Self Organizing Maps (SOM) [15]	DED	Ti-6Al-4V	Porosity	X-ray CT scans to locate the pores	Melt pool images	Temperature distributions of the melt pool top surface and its geometry	Acc = 96%
K-Nearest Neighbors (clustering) [23]	DED	Ti-6Al-4V	Porosity	X-ray CT scans	Melt pool images	Melt pool geometry such as Circumference, Length, width, total area	Acc = 98.4%
Convolutional Neural Networks [24]	DED	Sponge Titanium powder	Porosity	X-ray CT scans	Melt pool images	Melt pool geometry such as total area, eccentricity and extent.	Porosity Detection Acc = 91.2%. Volume prediction MSE = 1.32
Residual Recurrent CNN [22]	DED	Ti-6Al-4V	Porosity	Pore size measured using X-ray CT scans and 3D reconstructions	HAZ images from pyrometer and infrared camera	Melt pool geometry and temperature distributions	Acc = 99.49% Inference time = 8.67 ms
Long-term recurrent CNN [45]	DED	Ti-6Al-4V	Porosity	X-ray CT scans	Thermal Images from pyrometer & infrared camera	Pixels from melt pool images	Acc = 92.07%
Random Forest [46]	DED	Al-5083	Porosity	Visual inspection on optical micrographs: micropores, macropores and elongated pores	Optical micrographs	Geometry of pores from image processing such as perimeter, image texture, total area, circularity, etc.	Acc = 94.41%
Quadratic Discriminant Analysis (QDA) and SOM [47]	DED	Al-5083	Porosity	Visual Inspection on Optical micrographs	Optical micrographs	Geometric features of pores such as total area of pore (pixels), eccentricity, solidity, perimeter, etc.	Acc = 95%
K-means clustering [28]	DED	Ti-6Al-4V	Classify different manufacturing process conditions	Machine at inactive status, low laser power, low powder feed, etc.	Acoustic emission signals	Signal characteristics in the frequency domain	Acc = 86%
Logistic regression and ANN [27]	DED	Ti-6Al-4V, H13 (Tool Steel)	Pores and cracks	Optical microscope and SEM images	Acoustic emission signals	Peak amplitude, kurtosis, rise time, duration, energy, peak amplitude frequency	MSE (LR) = 1.73 MSE (ANN) = 1.70
Spectral CNN [26]	SLM	CL20ES stainless steel	Porosity	Optical Microscope images	Acoustic emission signals	Wavelet decomposition and energies of frequency bands	Acc = 89%
Process Monitoring [29]	SLM	Hastelloy X	Pores and microcracks	X-ray CT scans	Acoustic emission signals (Wireless transmission)	Signal characteristics in time 7 frequency domain	–
Spatial Gaussian process model [48]	SLM	17-4 PH stainless steel	Predict porosity or resulting density of AM part	Density measured as per Archimedes principle (ASTM – B962-14)	SLM printing process parameters	Laser power and scan speed at various locations within a bounded region	Mean squared prediction error MSPE = 0.2593
Bayesian Classification [49]	SLM	Inconel 625	Porosity	Visual Inspection of Camera Images	High resolution visual camera Images	Spectral features of image in the frequency domain.	Acc = 89.5%
Geometry - based simulation [25]	SLM	AlSi10Mg, Steel, TiAl6V4	Lack of fusion porosity	Experimental density data	SLM printing process parameters	Melt pool shape, laser power, layer thickness, scan speed & hatch spacing	–
Process Optimization Tool <i>DMP Meltpool</i> [50]	SLM	Ti-6Al-4V	Lack of fusion porosity	Density measurements per Archimedes principle and X-ray CT scans	Melt pool monitoring signals acquired by <i>DMP Melt pool</i>	–	Prediction sensitivity = 90%